

# Orbital Torque: Torque Generation by Orbital Current Injection

Dongwook Go<sup>1,2,3</sup> and Hyun-Woo Lee<sup>1,\*</sup>

<sup>1</sup>Department of Physics, Pohang University of Science and Technology, Pohang 37673, Korea

<sup>2</sup>Basic Science Research Institute, Pohang University of Science and Technology, Pohang 37673, Korea

<sup>3</sup>Peter GrÄijnberg Institut and Institute for Advanced Simulation, Forschungszentrum JÄijlich and JARA, 52425 JÄijlich, Germany

We propose a mechanism of torque generation by injection of an orbital current, which we call *orbital torque*. In a magnetic bilayer consisting of a nonmagnet (NM) and a ferromagnet (FM), we consider a situation where the spin-orbit coupling (SOC) is present only in the FM. Although the SOC is absent in the NM, the orbital Hall effect can arise in the NM. When the resulting orbital Hall current is injected to the FM, the SOC of the FM converts the orbital angular momentum into spin, which exerts torque to the magnetization of the FM. Remarkably, even for small SOC strength comparable to that of *3d* FMs, the orbital torque can be comparable to the spin torque induced by the spin Hall effect of the NM with strong SOC. This provides a way to experimentally probe the OHE and opens a new venue to achieving spin-torque devices based on light elements that exhibit gigantic orbital response. Experimental implications are discussed.

Spin injection into a ferromagnet (FM) generates a spin torque (ST) on magnetic moments of the FM by the angular momentum transfer from the spin of injected conduction electrons. For ST generation, a spin current source is needed. A popular source is a nonmagnet (NM) with strong spin-orbit coupling (SOC), which exhibits sizable spin Hall effect (SHE). The ST of the SOC origin is called spin-orbit torque [1–18], which has drawn considerable attention as a powerful means to electrically control magnetic configurations.

Similar to the SHE, the orbital Hall effect (OHE) allows for electrical generation of a transverse orbital current. In transition metals, for example, electron wavefunctions near atomic cores have mainly *d* character, and superpositions such as  $d_{zx} \pm id_{yz}$  carry the orbital angular momentum  $L_z = \pm\hbar$ . A flow of wavepackets with such superposed wavefunctions generates an orbital current. Considering that an orbital current carries the angular momentum just like a spin current does, it is reasonable to expect that injection of an orbital current (or orbital injection in short) into a FM may generate a torque on local magnetic moments of the FM. We call such torque as *orbital torque* (OT), which provides an experimental way to detect the OHE. Although the OHE has not yet been experimentally verified, theoretical calculations [19, 20] on *4d* and *5d* transition metals indicate that the orbital Hall conductivities (OHCs) of these NM's are about an order of magnitude larger than the spin Hall conductivities (SHCs). Moreover, our recent theoretical analysis finds that the OHC can be gigantic  $\sigma_{OH} \sim 10^4(\hbar/2|e|)(\Omega \cdot \text{cm})^{-1}$  even in materials with negligible SOC [21, 22]. Thus the OT also provides a new venue to achieving high torque efficiency in spintronic devices.

In this Letter, we investigate the theoretical idea of the OT for a NM/FM bilayer structure (Fig. 1). When an in-plane electric field  $\mathcal{E}$  is applied, both OHE and SHE arise in the NM in general [19–22]. In order to focus on the OT due to the orbital injection, we suppress the SHE by setting the SOC of the NM zero. Then only OHE is induced and a resulting torque in the FM can be identified unambiguously as the OT. We find that the OT indeed arises as long as the SOC of the

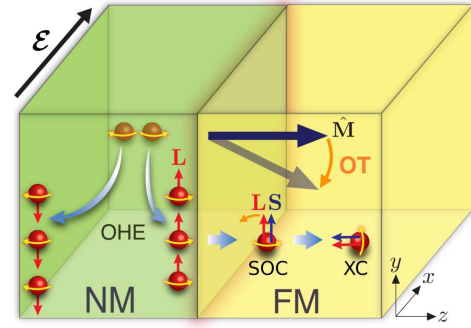


FIG. 1. Schematic illustration of the OT in a NM/FM bilayer. The orbital Hall current generated in the NM flows into the FM. The SOC of the FM then converts the orbital angular momentum to the spin, which exerts torque to the magnetization  $\hat{M}$ .

FM is finite.

For a quantitative evaluation of the OT, we adopt the tight-binding description of the bilayer with  $N_{\text{NM}}(N_{\text{FM}})$  atomic layer thick NM(FM) [Fig. 2(a)]. We assume both NM and FM to have the simple cubic structure. For the NM, we adopt the *sp* model that has been used previously [21] to illustrate the OHE without the SOC. In this model, each lattice site can host *s*,  $p_x$ ,  $p_y$ , and  $p_z$  orbitals, and the orbital hybridization, which is crucial for the emergence of the OHE [21], arises from the symmetry-allowed nearest neighbor hoppings between *s* and  $p_{x,y,z}$  orbitals. For the FM, we adopt a trivial *d* model; each lattice site can host  $d_{xy}$ ,  $d_{yz}$ ,  $d_{zx}$ ,  $d_{z^2}$ , and  $d_{x^2-y^2}$  orbitals with nearest neighboring hoppings allowed. This *d* model does not allow any orbital hybridization [23] and thus there is no OHE [21, 22]. The *d* model is augmented by adding the SOC

$$H_{\text{so}}^{\text{FM}} = \frac{\alpha_{\text{so}}^{\text{FM}}}{\hbar^2} \mathbf{L} \cdot \mathbf{S}, \quad (1)$$

and the exchange coupling  $H_{\text{xc}}^{\text{FM}} = (J/\hbar) \hat{M} \cdot \mathbf{S}$ , where  $\mathbf{L}$  is the orbital angular momentum of *d* character states in the FM,  $\mathbf{S}$  is the spin, and  $\hat{M}$  denotes the magnetization direction of the FM. Below, we focus on the case  $\hat{M} = \hat{z}$ . At the

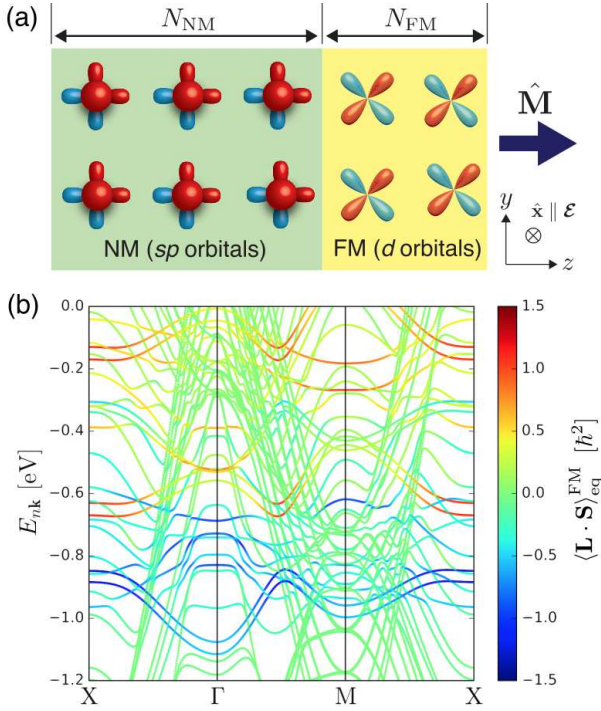


FIG. 2. (a) Schematic illustration of the tight-binding model of the NM/FM bilayer. (b) The band structure of the bilayer for  $N_{\text{NM}} = 8$  and  $N_{\text{FM}} = 2$ . The color represents the equilibrium expectation value of the spin-orbit correlation in the FM region  $\langle \mathbf{L} \cdot \mathbf{S} \rangle_{\text{eq}}^{\text{FM}}$  for each state.

interface, the nearest neighbor hoppings exist between the  $sp$  orbitals in the NM and the  $d$  orbitals in the FM. Details of the tight-binding description are given in Ref. [24]. All parameters of the NM and FM are set to have typical energy scales of nonmagnetic and magnetic metals. In particular, we set  $\alpha_{\text{so}}^{\text{FM}} = 100$  meV, which is a typical SOC strength of  $3d$  transition metals [22, 25, 26]. We emphasize that the nonzero  $\alpha_{\text{so}}^{\text{FM}}$  is crucial for the OT since  $\hat{\mathbf{M}}$  couples only to  $\mathbf{S}$  and there is no direct coupling between  $\hat{\mathbf{M}}$  and  $\mathbf{L}$  in the Hamiltonian. Thus for the injected orbital current to generate the OT, it should be first converted to spin through  $H_{\text{so}}^{\text{FM}}$  and then the resulting spin can generate the torque through  $H_{\text{xc}}^{\text{FM}}$  (Fig. 1).

Figure 2(b) shows the band structure of the NM/FM bilayer for  $N_{\text{NM}} = 8$  and  $N_{\text{FM}} = 2$ , where the color represents the equilibrium expectation value of the spin-orbit correlation in the FM region  $\langle \mathbf{L} \cdot \mathbf{S} \rangle_{\text{eq}}^{\text{FM}}$  for each state. The correlation is negative in the lower energy range ( $-1.1$  eV  $< E_{n\mathbf{k}} < -0.7$  eV), and positive in the higher energy range ( $-0.3$  eV  $< E_{n\mathbf{k}} < +0.2$  eV). In the middle energy range ( $-0.7$  eV  $< E_{n\mathbf{k}} < -0.3$  eV), states with positive and negative correlations coexist. We later demonstrate that  $\langle \mathbf{L} \cdot \mathbf{S} \rangle_{\text{eq}}^{\text{FM}}$  is important for the sign of the OT.

For  $\mathcal{E} = \mathcal{E}_x \hat{x}$ , we calculate the electrically generated orbital ( $\mathbf{L}$ ) and spin ( $\mathbf{S}$ ) accumulations at each atomic layer as a function of  $z$ . From the Kubo formula, one obtains the expectation value  $\langle \mathbf{X}(z) \rangle = \langle \mathbf{X}(z) \rangle^{\text{intra}} + \langle \mathbf{X}(z) \rangle^{\text{inter}}$  ( $\mathbf{X} = \mathbf{L}$  or

$\mathbf{S}$ ) generated by  $\mathcal{E}_x$ , where

$$\langle \mathbf{X}(z) \rangle^{\text{intra}} = \frac{e\hbar\mathcal{E}_x}{2\Gamma} \sum_n \int \frac{d^2k}{(2\pi)^2} f'_{n\mathbf{k}} \times \text{Re} [\langle u_{n\mathbf{k}} | \mathbf{X}(z) | u_{n\mathbf{k}} \rangle \langle u_{n\mathbf{k}} | v_x | u_{n\mathbf{k}} \rangle], \quad (2a)$$

$$\langle \mathbf{X}(z) \rangle^{\text{inter}} = -e\hbar\mathcal{E}_x \sum_{nm} \int \frac{d^2k}{(2\pi)^2} (f_{n\mathbf{k}} - f_{m\mathbf{k}}) \times \text{Im} \left[ \frac{\langle u_{n\mathbf{k}} | \mathbf{X}(z) | u_{m\mathbf{k}} \rangle \langle u_{m\mathbf{k}} | v_x | u_{n\mathbf{k}} \rangle}{(E_{n\mathbf{k}} - E_{m\mathbf{k}} + i\Gamma)^2} \right], \quad (2b)$$

are the intraband and interband contributions, respectively. Here,  $\mathbf{X}(z) = P(z)\mathbf{X}P(z)$  measures the local accumulation of  $\mathbf{X}$  at  $z$ , where  $P(z)$  is the projection operator to the atomic layer at  $z$ . In Eq. (2),  $e > 0$  is the unit charge,  $\hbar$  is the Planck constant,  $v_x$  is the velocity operator along the  $\hat{x}$  direction,  $f_{n\mathbf{k}}$  is the Fermi-Dirac distribution function for a periodic part of the Bloch state  $|u_{n\mathbf{k}}\rangle$  with its energy eigenvalue  $E_{n\mathbf{k}}$ . To incorporate the effect of disorder scatterings, we phenomenologically introduce a spectral broadening  $\Gamma = 25$  meV, which is a room temperature scale.

Figure 3 shows the (a)  $y$  and (b)  $x$  components of the resulting  $\langle \mathbf{L}(z) \rangle$  and  $\langle \mathbf{S}(z) \rangle$  for the Fermi energy  $E_{\text{F}} = -0.9$  eV. We first consider a situation when the NM and the FM are disconnected (hoppings between the NM and FM turned off). In the NM ( $1 \leq z \leq 20$ ),  $\langle L_y(z) \rangle$  [white inverted triangles in Fig. 3(a)] has nonzero values of opposite signs at the opposite edges of the NM ( $z = 1$  and  $20$ ). This result can be interpreted as the orbital accumulation at the edges due to the OHE in the NM. The OHC in the NM is  $\sigma_{\text{OH}} \approx 2,000 (\hbar/2|e|)(\Omega \cdot \text{cm})^{-1}$  for  $E_{\text{F}} = -0.9$  eV [21, 24]. On the other hand,  $\langle L_x(z) \rangle$  [white inverted triangles in Fig. 3(b)] is absent in the NM. In the FM ( $21 \leq z \leq 30$ ), both  $\langle L_x(z) \rangle$  and  $\langle L_y(z) \rangle$  are zero, confirming the absence of the OHE in the FM. The spin accumulation is zero both in the NM and the FM (not shown), which is natural since the SHE is absent in both NM and FM.

Next we connect the NM and the FM (hoppings between the NM and FM turned on). Near  $z = 1$ , which is far from the NM/FM interface,  $\langle L_y(z) \rangle$  [blue circles in Fig 3(a)] remains essentially unchanged. Near the interface ( $z = 20$ ), on the other hand,  $\langle L_y(z) \rangle$  is reduced significantly since the orbital Hall current is now injected into the FM instead of getting accumulated at the interface. The injected orbital Hall current in the FM produces not only  $\langle L_y(z) \rangle$  but also  $\langle S_y(z) \rangle$  [orange squares in Fig 3(a) for  $10\times$  enlarged values] due to  $H_{\text{so}}^{\text{FM}}$ . Moreover once  $\langle S_y(z) \rangle$  becomes nonzero in the FM, the spin precesses around  $\hat{\mathbf{M}}$  due to  $H_{\text{xc}}^{\text{FM}}$  and produces  $\langle S_x(z) \rangle$  as well [orange squares in Fig 3(b) for  $10\times$  enlarged values]. This precession results in oscillatory profiles of  $\langle S_y(z) \rangle$  and  $\langle S_x(z) \rangle$  in the FM, which resemble oscillatory spin accumulation profiles [9] in a conventional situation, where a *spin* current is injected into a FM to generate the ST. The oscillatory profiles of  $\langle S_x(z) \rangle$  and  $\langle S_y(z) \rangle$  in the FM are accompanied by similar oscillatory profiles of  $\langle L_x(z) \rangle$  and  $\langle L_y(z) \rangle$ . The coexistence of the spin and orbital accumulation oscillations

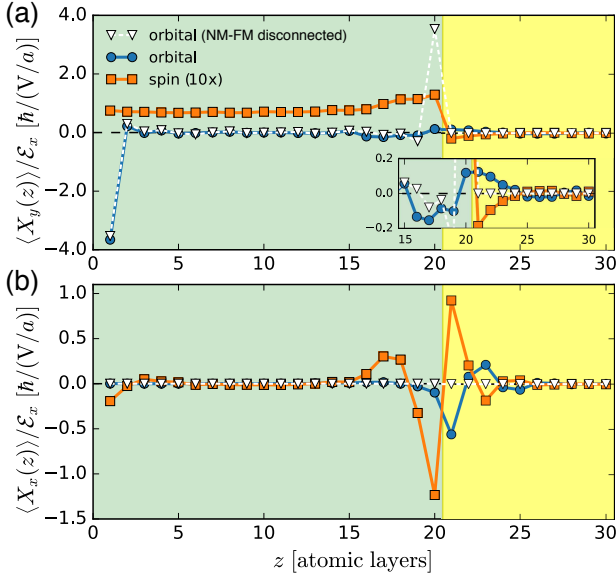


FIG. 3. (a)  $\langle X_y(z) \rangle / \mathcal{E}_x$  and (b)  $\langle X_x(z) \rangle / \mathcal{E}_x$  as a function of  $z$  for  $E_F = -0.9$  eV. Blue circles (orange squares) depict the orbital (spin multiplied by factor 10) accumulation profile in the NM ( $1 \leq z \leq 20$ ) and the FM ( $21 \leq z \leq 30$ ). White inverted triangles depict the orbital accumulation profile when the NM and FM are disconnected. The inset in (a) presents a magnified plot near the NM/FM interface.

is due to  $H_{\text{so}}^{\text{FM}}$  and we note that the spin and orbital oscillations are  $180^\circ$  out of phase for  $E_F = -0.9$  eV (Fig. 3), which we attribute to negative spin-orbit correlation at this energy [Fig. 2(b)]. By the way, the spin accumulation in the NM is due to partial reflection of the orbital Hall current at the NM/FM interface.

The torque  $\mathbf{T}$  acting on the FM can be obtained from the spin accumulation as follows,

$$\mathbf{T} = \frac{J}{\hbar} \hat{\mathbf{M}} \times \langle \mathbf{S} \rangle^{\text{FM}}, \quad (3)$$

where  $\langle \mathbf{S} \rangle^{\text{FM}} = \sum_{z \in \text{FM}} \langle \mathbf{S}(z) \rangle$ . When the SOC of the NM is zero,  $\mathbf{T}$  arises from the orbital injection and thus the resulting  $\mathbf{T}$  amounts to the OT. Analogous to the ST, the OT can be decomposed as  $\mathbf{T} = \tau_f \hat{\mathbf{M}} \times \hat{\mathbf{y}} + \tau_d \hat{\mathbf{M}} \times (\hat{\mathbf{M}} \times \hat{\mathbf{y}})$ , where  $\tau_{f(d)}$  refers to the field(damping)-like component. When  $\hat{\mathbf{M}} = \hat{\mathbf{z}}$ ,  $\tau_f = (J/\hbar) \langle S_y \rangle^{\text{FM}}$  and  $\tau_d = -(J/\hbar) \langle S_x \rangle^{\text{FM}}$ . We find that  $\langle S_{y(x)}(z) \rangle$ , which arises from the intraband(interband) contribution in Eq. (2), is even(odd) in  $\hat{\mathbf{M}}$ , thus the field(damping)-like OT is odd(even) under sign reversal of  $\hat{\mathbf{M}}$ . This is similar to the generation of the field-like and damping-like STs when a spin current polarized along  $\hat{\mathbf{y}}$  direction is injected into a FM magnetized along the  $\hat{\mathbf{z}}$  direction [9].

Since  $\tau_d$  plays a more important role for the current-induced magnetization dynamics than  $\tau_f$  [6, 7], we focus on  $\langle S_x \rangle^{\text{FM}}$ . A result for  $\langle S_y \rangle^{\text{FM}}$  is given in Ref. [24]. Figure 4(a) shows that the ratio  $\langle S_x \rangle^{\text{FM}} / \mathcal{E}_x$  (orange squares) is positive for  $-1.0 \text{ eV} \lesssim E_F \lesssim -0.6 \text{ eV}$  and negative for  $-0.2 \text{ eV} \lesssim E_F \lesssim 0.0 \text{ eV}$ . For comparison, the ratio  $\langle L_x \rangle^{\text{FM}} / \mathcal{E}_x$  (blue circles) is also shown, where  $\langle L_x \rangle^{\text{FM}} \equiv \sum_{z \in \text{FM}} \langle L_x(z) \rangle$ .

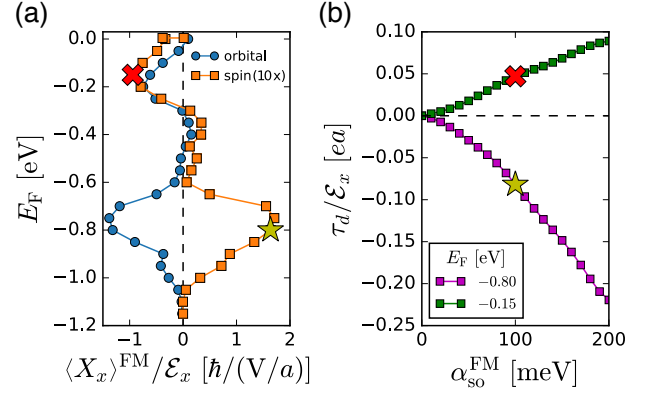


FIG. 4. (a)  $\langle S_x \rangle^{\text{FM}} / \mathcal{E}_x$  (orange squares for  $10\times$  magnified values) as a function of  $E_F$  with  $\alpha_{\text{so}}^{\text{FM}} = 100$  meV. For comparison,  $\langle L_x \rangle^{\text{FM}} / \mathcal{E}_x$  (blue circles) is also shown. (b)  $\tau_d / \mathcal{E}_x$  as a function of  $\alpha_{\text{so}}^{\text{FM}}$  with  $E_F = -0.80$  eV (purple squares) and  $E_F = -0.15$  eV (green squares). The yellow star and red cross symbols in (a) and (b) are obtained for the same  $E_F$  and  $\alpha_{\text{so}}^{\text{FM}}$ . For this calculation, smaller system size is used ( $N_{\text{NM}} = 8$  and  $N_{\text{FM}} = 2$ ).

Note that the relative ratio between  $\langle S_x \rangle^{\text{FM}}$  and  $\langle L_x \rangle^{\text{FM}}$  is negative for  $-1.0 \text{ eV} \lesssim E_F \lesssim -0.6 \text{ eV}$ , and positive for  $-0.2 \text{ eV} \lesssim E_F \lesssim 0.0 \text{ eV}$ . The  $E_F$ -dependence of the relative ratio sign closely resembles the energy dependence of the spin-orbit correlation  $\langle \mathbf{L} \cdot \mathbf{S} \rangle_{\text{eq}}^{\text{FM}}$  in Fig. 2(b). By combining the calculation result in Fig. 4(a) with the fact that the OHC of the NM is positive essentially for all  $E_F$  [21], we find that the sign of  $\langle S_x \rangle^{\text{FM}} / \mathcal{E}_x$  tends to be determined by the sign of the product between the OHC of the NM and the spin-orbit correlation in the FM. Considering that  $\langle S_x \rangle^{\text{FM}}$  determines the damping-like OT, the latter tendency may be regarded as the OT counterpart of the sign “rule” for the ST; the damping-like ST tends to be determined by the sign of the spin Hall conductivity (SHC) in the NM [6, 7, 9].

Figure 4(b) shows the ratio  $\tau_d / \mathcal{E}_x$  as a function of  $\alpha_{\text{so}}^{\text{FM}}$  for  $E_F = -0.80$  eV (purple squares) and  $E_F = -0.15$  eV (green squares). These two  $E_F$  values are close to the peak positions in Fig. 4(a) (denoted by the yellow star and the red cross). For these favorable choices of  $E_F$ , values of  $\tau_d / \mathcal{E}_x$  are  $-0.08 ea$  and  $+0.05 ea$  for  $\alpha_{\text{so}}^{\text{FM}} = 100$  meV, which is SOC energy scale for  $3d$  FMs. Here  $a$  is the lattice constant. By increasing  $\alpha_{\text{so}}^{\text{FM}}$ , they reach up to  $-0.22 ea$  and  $+0.09 ea$  for  $\alpha_{\text{so}}^{\text{FM}} = 200$  meV, which is SOC energy scale for  $4d$  transition metals. Note that these values  $\tau_d / \mathcal{E}_x \sim 0.1 ea$  for  $\alpha_{\text{so}}^{\text{FM}} = 100, 200$  meV are not negligible compared to the corresponding value  $\sim 0.5 ea$  for the damping-like torque calculated for the Pt/Co bilayer [18, 27] with the SOC strength of  $500$  meV for Pt. Then, considering that the OHC in real materials such as V is gigantic  $\sigma_{\text{OH}} \sim 12,000 (\hbar/2|e|)(\Omega \cdot \text{cm})^{-1}$ , which is about 6 times larger than the OHC of the  $sp$  model used in our calculation,  $\tau_d / \mathcal{E}_x$  for real NMs may be proportionally larger and comparable to the corresponding ST value for the Pt/Co bilayer. Although quantitative predictions on  $\tau_d / \mathcal{E}_x$  require realistic calculations that take material details into account, we argue it is still reasonable to expect that the



	$\langle \mathbf{L} \cdot \mathbf{S} \rangle_{\text{eq}}^{\text{FM}} > 0$	$\langle \mathbf{L} \cdot \mathbf{S} \rangle_{\text{eq}}^{\text{FM}} < 0$
$\langle \mathbf{L} \cdot \mathbf{S} \rangle_{\text{eq}}^{\text{NM}} > 0$	same sign	opposite signs
$\langle \mathbf{L} \cdot \mathbf{S} \rangle_{\text{eq}}^{\text{NM}} < 0$	opposite signs	same sign

TABLE I. Relative signs of the OT and ST depending on the spin-orbit correlations in the NM and FM.

OT may be sizable for a FM with weak SOC, thus providing an alternative route to enhancing the torque efficiency.

So far we have assumed the SOC is absent in the NM. Now we consider a situation where not only the FM but also the NM have the SOC. Thus the *sp* model Hamiltonian for the NM now includes

$$H_{\text{so}}^{\text{NM}} = \frac{\alpha_{\text{so}}^{\text{NM}}}{\hbar^2} \mathbf{L} \cdot \mathbf{S}, \quad (4)$$

where  $\alpha_{\text{so}}^{\text{NM}}$  is the SOC parameter in the NM. Since *s* character states do not carry the orbital angular momentum,  $\mathbf{L}$  in Eq. (S23) acts only on *p* character states. Due to  $H_{\text{so}}^{\text{NM}}$ , the NM exhibits SHE, as well as the OHE. Thus, on top of the OT, injection of the spin Hall current into the FM generates the ST. It is known that OHE and SHE occur in the same(opposite) direction if  $\langle \mathbf{L} \cdot \mathbf{S} \rangle_{\text{eq}}^{\text{NM}}$  is positive(negative) at  $E_{\text{F}}$  [19–21]. Thus, when  $\langle \mathbf{L} \cdot \mathbf{S} \rangle_{\text{eq}}^{\text{FM}} > 0$  at  $E_{\text{F}}$ , which is a case for Ni, the OT and ST add up if  $\langle \mathbf{L} \cdot \mathbf{S} \rangle_{\text{eq}}^{\text{NM}} > 0$  and cancel each other if  $\langle \mathbf{L} \cdot \mathbf{S} \rangle_{\text{eq}}^{\text{NM}} < 0$ . This situation becomes the opposite when  $\langle \mathbf{L} \cdot \mathbf{S} \rangle_{\text{eq}}^{\text{FM}} < 0$ , as in Gd. The result is summarized in Table I, which is supported by our numerical calculation [24]. This implies that the total torque may go even beyond the level expected from the theoretical value for the SHC of a NM, as in recent experiments [28, 29] When the OT and ST cancel each other, the total torque may even exhibit the opposite sign compared to the sign expected from the SHC of the NM. For example, Ta and W exhibit the opposite signs of the OHC and SHC [19].

Unfortunately, the OT and ST exhibit *qualitatively* similar behavior, thus disentangling the OT from the ST is challenging. The orbital and spin operator transform in the same way for symmetry operations, i.e. both OT and ST exhibit the same angular dependence. Nonetheless, the OT and ST are expected to exhibit different *quantitative* features. One characteristic feature of the OT is its strong correlation with  $\langle \mathbf{L} \cdot \mathbf{S} \rangle_{\text{eq}}^{\text{FM}}$  as demonstrated in Figs. 3 and 4(b). This suggests that the OT can be probed through material variation of a FM. This is in stark contrast to the ST, where the a role of the FM is less important. We expect that alloying a FM with heavy elements would not only increase the OT since the conversion from the orbital to spin becomes more efficient but also provide a way to systematically tune the spin-orbit correlation of the FM [30].

Another distinct feature of the OT compared to the ST is its dependence on the interface crystallinity. For the orbital injection across the interface, it must occur through orbital hybridizations at the NM/FM interface. In the tight-binding model in Fig. 2(a),  $p_z^{\text{NM}} - d_{z^2-x^2}^{\text{FM}}$  and  $p_x^{\text{NM}} - d_{zx}^{\text{FM}}$  hybridizations are crucial for transferring  $\langle L_y \rangle$  [24]. Thus even

spin-conserving interface scatterings can result in orbital relaxation, making the *orbital transparency* more sensitive to the interface crystallinity than the spin transparency. Particularly, when the NM and FM elements tend to be mixed, the OT will be suppressed since the atomic ordering of the NM and FM atoms disappears at the interface [31].

When the NM/FM bilayer consists only of light elements with weak SOC, the total torque is dominated by the OT as in Fig. 1, which is advantageous for unambiguously quantifying the OT. In the past, unexpectedly large torque was measured in samples containing Cr [32, 33] and Py [34, 35] in spite of small SOC of these elements. These results may be related to the OT, which requires further investigation. Finally, we remark that the orbital angular momentum can be generated not only by the OHE but also by the interfacial Rashba-type states [36, 37], which may be related to sizable field-like torque measured in Py/(Cu)/AlO<sub>x</sub> structure [38].

We acknowledge Daegeun Jo, Junyeon Kim, YoshiChika Otani, Jan-Philipp Hanke, Frank Freimuth, Yuriy Mokrousov, and Kyung-Jin Lee for insightful discussions. D. G. and H.-W. L. were supported by the SSTF (Grant No. BA-1501-07).

\* hwl@postech.ac.kr

- [1] Ung Hwan Pi, Kee Won Kim, Ji Young Bae, Sung Chul Lee, Young Jin Cho, Kwang Seok Kim, and Sunae Seo, “Tilting of the spin orientation induced by Rashba effect in ferromagnetic metal layer,” Appl. Phys. Lett. **97**, 162507 (2010).
- [2] Ioan Mihai Miron, Gilles Gaudin, Stéphane Auffret, Bernard Rodmacq, Alain Schuhl, Stefania Pizzini, Jan Vogel, and Pietro Gambardella, “Current-driven spin torque induced by the rashba effect in a ferromagnetic metal layer,” Nat. Mater. **9**, 230 (2010).
- [3] Ioan Mihai Miron, Thomas Moore, Helga Szabolics, Liliana Daniela Buda-Prejbeanu, Stéphane Auffret, Bernard Rodmacq, Stefania Pizzini, Jan Vogel, Marlio Bonfim, Alain Schuhl, and Gilles Gaudin, “Fast current-induced domain-wall motion controlled by the rashba effect,” Mat. Mater. **10**, 419 (2011).
- [4] Ioan Mihai Miron, Kevin Garello, Gilles Gaudin, Pierre-Jean Zermatten, Marius V. Costache, Stéphane Auffret, Sébastien Bandiera, Bernard Rodmacq, Alain Schuhl, and Pietro Gambardella, “Perpendicular switching of a single ferromagnetic layer induced by in-plane current injection,” Nature (London) **476**, 189 (2011).
- [5] Chi-Feng Pai, Luqiao Liu, Y. Li, H. W. Tseng, D. C. Ralph, and R. A. Buhrman, “Spin transfer torque devices utilizing the giant spin Hall effect of tungsten,” Applied Physics Letters **101**, 122404 (2012).
- [6] Luqiao Liu, O. J. Lee, T. J. Gudmundsen, D. C. Ralph, and R. A. Buhrman, “Current-Induced Switching of Perpendicularly Magnetized Magnetic Layers Using Spin Torque from the Spin Hall Effect,” Phys. Rev. Lett. **109**, 096602 (2012).
- [7] Luqiao Liu, Chi-Feng Pai, Y. Li, H. W. Tseng, D. C. Ralph, and R. A. Buhrman, “Spin-Torque Switching with the Giant Spin Hall Effect of Tantalum,” Science **336**, 555–558 (2012).
- [8] Kyoung-Wan Kim, Soo-Man Seo, Jisu Ryu, Kyung-Jin Lee, and Hyun-Woo Lee, “Magnetization dynamics induced by in-plane currents in ultrathin magnetic nanostructures with rashba

- spin-orbit coupling,” *Phys. Rev. B* **85**, 180404(R) (2012).
- [9] Paul M. Haney, Hyun-Woo Lee, Kyung-Jin Lee, Aurélien Manchon, and M. D. Stiles, “Current induced torques and interfacial spin-orbit coupling: Semiclassical modeling,” *Phys. Rev. B* **87**, 174411 (2013).
- [10] Paul M. Haney, Hyun-Woo Lee, Kyung-Jin Lee, Aurélien Manchon, and M. D. Stiles, “Current-induced torques and interfacial spin-orbit coupling,” *Phys. Rev. B* **88**, 214417 (2013).
- [11] Kevin Garello, Ioan Mihai Miron, Can Onur Avci, Frank Freimuth, Yuriy Mokrousov, Stefan Blügel, Stéphane Auffret, Olivier Boulle, Gilles Gaudin, and Pietro Gambardella, “Symmetry and magnitude of spin-orbit torques in ferromagnetic heterostructures,” *Nat. Nanotechnol.* **8**, 587 (2013).
- [12] Kevin Garello, Can Onur Avci, Ioan Mihai Miron, Manuel Baumgartner, Abhijit Ghosh, Stéphane Auffret, Olivier Boulle, Gilles Gaudin, and Pietro Gambardella, “Ultrafast magnetization switching by spin-orbit torques,” *Applied Physics Letters* **105**, 212402 (2014).
- [13] H. Kurebayashi, Jairo Sinova, D. Fang, A. C. Irvine, T. D. Skinner, J. Wunderlich, V. Novák, R. P. Campion, B. L. Gallagher, E. K. Vehstedt, L. P. Zárbo, K. Výborný, A. J. Ferguson, and T. Jungwirth, “An antidamping spin-orbit torque originating from the Berry curvature,” *Nat. Nanotechnol.* **9**, 211 (2014), article.
- [14] Masamitsu Hayashi, Junyeon Kim, Michihiko Yamanouchi, and Hideo Ohno, “Quantitative characterization of the spin-orbit torque using harmonic Hall voltage measurements,” *Phys. Rev. B* **89**, 144425 (2014).
- [15] Guoqiang Yu, Pramey Upadhyaya, Yabin Fan, Juan G. Alzate, Wanjun Jiang, Kin L. Wong, So Takei, Scott A. Bender, Li-Te Chang, Ying Jiang, Murong Lang, Jianshi Tang, Yong Wang, Yaroslav Tserkovnyak, Pedram Khalili Amiri, and Kang L. Wang, “Switching of perpendicular magnetization by spin-orbit torques in the absence of external magnetic fields,” *Nat. Nanotechnol.* **9**, 548 (2014).
- [16] Frank Freimuth, Stefan Blügel, and Yuriy Mokrousov, “Spin-orbit torques in Co/Pt(111) and Mn/W(001) magnetic bilayers from first principles,” *Phys. Rev. B* **90**, 174423 (2014).
- [17] Kyoung-Whan Kim, Kyung-Jin Lee, Jairo Sinova, Hyun-Woo Lee, and M. D. Stiles, “Spin-orbit torques from interfacial spin-orbit coupling for various interfaces,” *Phys. Rev. B* **96**, 104438 (2017).
- [18] Farzad Mahfouzi and Nicholas Kioussis, “First-principles study of the angular dependence of the spin-orbit torque in Pt/Co and Pd/Co bilayers,” *Phys. Rev. B* **97**, 224426 (2018).
- [19] T. Tanaka, H. Kontani, M. Naito, T. Naito, D. S. Hirashima, K. Yamada, and J. Inoue, “Intrinsic spin Hall effect and orbital Hall effect in  $4d$  and  $5d$  transition metals,” *Phys. Rev. B* **77**, 165117 (2008).
- [20] H. Kontani, T. Tanaka, D. S. Hirashima, K. Yamada, and J. Inoue, “Giant Orbital Hall Effect in Transition Metals: Origin of Large Spin and Anomalous Hall Effects,” *Phys. Rev. Lett.* **102**, 016601 (2009).
- [21] Dongwook Go, Daegeun Jo, Changyoung Kim, and Hyun-Woo Lee, “Intrinsic Spin and Orbital Hall Effects from Orbital Texture,” *Phys. Rev. Lett.* **121**, 086602 (2018).
- [22] Daegeun Jo, Dongwook Go, and Hyun-Woo Lee, “Gigantic intrinsic orbital hall effects in weakly spin-orbit coupled metals,” *Phys. Rev. B* **98**, 214405 (2018).
- [23] The OHE arises in more realistic  $d$  models that take into account one of the following complexities; next-nearest neighbor hopping, extra orbitals ( $s$  or  $p$ ), or non-simple-cubic structure.
- [24] See Supplementary Material.
- [25] C. S. Wang and J. Callaway, “Band structure of nickel: Spin-orbit coupling, the fermi surface, and the optical conductivity,” *Phys. Rev. B* **9**, 4897–4907 (1974).
- [26] Veronika Sunko, H. Rosner, P. Kushwaha, S. Khim, F. Mazzola, L. Bawden, O. J. Clark, J. M. Riley, D. Kasinathan, M. W. Haverkort, T. K. Kim, M. Hoesch, J. Fujii, I. Vobornik, A. P. Mackenzie, and P. D. C. King, “Maximal rashba-like spin splitting via kinetic-energy-coupled inversion-symmetry breaking,” *Nature* **549**, 492 (2017).
- [27] Frank Freimuth, Stefan Blügel, and Yuriy Mokrousov, “Anisotropic Spin Hall Effect from First Principles,” *Phys. Rev. Lett.* **105**, 246602 (2010).
- [28] Lijun Zhu, Daniel C. Ralph, and Robert A. Buhrman, “Highly Efficient Spin-Current Generation by the Spin Hall Effect in  $\text{Au}_{1-x}\text{Pt}_x$ ,” *Phys. Rev. Appl.* **10**, 031001 (2018).
- [29] Ye Du, Shutaro Karube, Hiromu Gamou, Jeongchun Ryu, Saburo Takahashi, Makoto Kohda, and Junsaku Nitta, “Anomalous spin orbit torques with large rashba spin orbit coupling in epitaxial Pt/Co bilayers,” (2018), arXiv:1807.10867.
- [30] Increasing the SOC in the FM may result in sizable SHE in the FM, as pointed out in Refs. [39, 40]. However, the SHE in the FM leads to an antisymmetric accumulation of the spin within the FM layer, leading to a non-uniform tilting of the magnetization. Thus, when the thickness of the FM is smaller than the spin diffusion length, this effect is expected to vanish. On the other hand, the OT mechanism proposed in this Letter is not affected by the thickness of the FM, and results in uniform tilting of the magnetization.
- [31] Note that the atomic ordering persists locally even in polycrystalline samples. However, at the interface mixing(demixing) nature of the NM and FM elements can suppress(enhance) the crystallinity dependence of the OT will be weaker.
- [32] Chunhui Du, Hailong Wang, Fengyuan Yang, and P. Chris Hammel, “Systematic variation of spin-orbit coupling with  $d$ -orbital filling: Large inverse spin hall effect in  $3d$  transition metals,” *Phys. Rev. B* **90**, 140407(R) (2014).
- [33] D. Qu, S. Y. Huang, and C. L. Chien, “Inverse spin hall effect in cr: Independence of antiferromagnetic ordering,” *Phys. Rev. B* **92**, 020418(R) (2015).
- [34] B. F. Miao, S. Y. Huang, D. Qu, and C. L. Chien, “Inverse Spin Hall Effect in a Ferromagnetic Metal,” *Phys. Rev. Lett.* **111**, 066602 (2013).
- [35] Ayaka Tsukahara, Yuichiro Ando, Yuta Kitamura, Hiroyuki Emoto, Eiji Shikoh, Michael P. Delmo, Teruya Shinjo, and Masashi Shiraiishi, “Self-induced inverse spin hall effect in permalloy at room temperature,” *Phys. Rev. B* **89**, 235317 (2014).
- [36] Dongwook Go, Jan-Philipp Hanke, Patrick M. Buhl, Frank Freimuth, Gustav Bihlmayer, Hyun-Woo Lee, Yuriy Mokrousov, and Stefan Blügel, “Toward surface orbitronics: giant orbital magnetism from the orbital rashba effect at the surface of sp-metals,” *Sci. Rep.* **7**, 46742 (2017).
- [37] Xi Chen, Yang Liu, Guang Yang, Hui Shi, Chen Hu, Minghua Li, and Haibo Zeng, “Giant antidamping orbital torque originating from the orbital Rashba-Edelstein effect in ferromagnetic heterostructures,” *Nat. Commun.* **9**, 2569 (2018).
- [38] Satoru Emori, Tianxiang Nan, Amine M. Belkessam, Xinjun Wang, Alexei D. Matyushov, Christopher J. Babroski, Yuan Gao, Hwaider Lin, and Nian X. Sun, “Interfacial spin-orbit torque without bulk spin-orbit coupling,” *Phys. Rev. B* **93**, 180402(R) (2016).
- [39] V. P. Amin, Junwen Li, M. D. Stiles, and P. M. Haney, “Intrinsic spin currents in ferromagnets,” *Phys. Rev. B* **99**, 220405 (2019).
- [40] W. Wang, T. Wang, V. P. Amin, Y. Wang, A. radhakrishnan,

A. Davidson, S. R. Allen, T. J. Silva, H. Ohldag, D. Balzar, B. L. Zink, P. M. Haney, J. Q. Xiao, D. G. Cahill, V. O. Lorenz, and X. Fan, "Anomalous spin-orbit torques in magnetic single-layer films," (2019), arXiv:1902.05490.

# Supplementary Material for “Orbital Torque: Torque Generation by Orbital Current Injection”

Dongwook Go and Hyun-Woo Lee\*

## CONTENTS

A. Tight-Binding Model	S1
1. NM	S1
2. FM	S2
3. Interface	S3
4. Parameter Setting	S4
B. Spatial Profiles of the Orbital and Spin Hall Currents	S4
C. Correlation between $\langle X_y \rangle^{\text{FM}}$ and $\langle X_x \rangle^{\text{FM}}$ ( $X = L, S$ ): Fermi Energy Dependence	S5
D. Spin-Orbit Coupling Dependence	S5
E. Orbital Torque versus Spin Torque	S6
1. NM SOC included	S6
2. NM SOC included, FM onsite changed	S8
F. Role of the Interface Hoppings for the Orbital Torque	S9
References	S10

### A. Tight-Binding Model

The tight-binding model for a magnetic bilayer presented in the Letter is composed of a nonmagnet (NM) and a ferromagnet (FM). The numbers of layers for the NM and the FM are  $N_{\text{NM}}$  and  $N_{\text{FM}}$ , respectively. We assume the simple cubic structure for both NM and FM with only nearest neighbor hoppings allowed. We also assume that the layer is periodic in  $x$  and  $y$  directions, and the layers are stacked along  $z$  direction. Thus, the NM is located from  $z = 1$  to  $z = N_{\text{NM}}$  and the FM is located from  $z = N_{\text{NM}} + 1$  to  $z = N_{\text{NM}} + N_{\text{FM}}$  (in unit of the lattice spacing  $a$ ), and we use the Bloch theorem for  $x$  and  $y$  directions by introducing the crystal momentum  $\mathbf{k} = (k_x, k_y)$ . The total Hamiltonian is formally written as

$$H_{\text{tot}}(\mathbf{k}) = \begin{pmatrix} H_{\text{NM}}^{2\text{d}}(\mathbf{k}) & T_{\text{NM}}^\dagger & \cdots & 0 & 0 & 0 & 0 & \cdots & 0 & 0 \\ T_{\text{NM}} & H_{\text{NM}}^{2\text{d}}(\mathbf{k}) & \cdots & 0 & 0 & 0 & 0 & \cdots & 0 & 0 \\ \vdots & \vdots & \ddots & \vdots & \vdots & \vdots & \vdots & \ddots & \vdots & \vdots \\ 0 & 0 & \cdots & H_{\text{NM}}^{2\text{d}}(\mathbf{k}) & T_{\text{NM}}^\dagger & 0 & 0 & \cdots & 0 & 0 \\ 0 & 0 & \cdots & T_{\text{NM}} & H_{\text{NM}}^{2\text{d}}(\mathbf{k}) & T_{\text{int}}^\dagger & 0 & \cdots & 0 & 0 \\ \hline 0 & 0 & \cdots & 0 & T_{\text{int}} & H_{\text{FM}}^{2\text{d}}(\mathbf{k}) & T_{\text{FM}}^\dagger & \cdots & 0 & 0 \\ 0 & 0 & \cdots & 0 & 0 & T_{\text{FM}} & H_{\text{FM}}^{2\text{d}}(\mathbf{k}) & \cdots & 0 & 0 \\ \vdots & \vdots & \ddots & \vdots & \vdots & \vdots & \vdots & \ddots & \vdots & \vdots \\ 0 & 0 & \cdots & 0 & 0 & 0 & 0 & \cdots & H_{\text{FM}}^{2\text{d}}(\mathbf{k}) & T_{\text{FM}}^\dagger \\ 0 & 0 & \cdots & 0 & 0 & 0 & 0 & \cdots & T_{\text{FM}} & H_{\text{FM}}^{2\text{d}}(\mathbf{k}) \end{pmatrix}, \quad (\text{S1})$$

where  $H_{\text{NM(FM)}}^{2\text{d}}(\mathbf{k})$  is the Hamiltonian for a two-dimensional NM(FM) layer,  $T_{\text{NM(FM)}}$  is the hopping between nearest NM(FM) layers, and  $T_{\text{int}}$  is the interface hopping between the last NM layer ( $z = N_{\text{NM}}$ ) and the first FM layer ( $z = N_{\text{NM}} + 1$ ).

#### 1. NM

We assume the NM hosts  $sp_\alpha$  ( $\alpha = x, y, z$ ) orbitals at each site, which was introduced in Ref. [S1]. Writing the Hamiltonian in a finite film structure is straightforward as follows. The Hamiltonian within each two-dimensional NM layer consists of the kinetic energy and spin-orbit coupling (SOC) parts:

$$H_{\text{NM}}^{2\text{d}}(\mathbf{k}) = H_{\text{NM}}^{\text{kin}}(\mathbf{k}) + H_{\text{NM}}^{\text{soc}}(\mathbf{k}). \quad (\text{S2})$$

First, the kinetic part is

$$H_{\text{NM}}^{\text{kin}}(\mathbf{k}) = \begin{pmatrix} E_s(\mathbf{k}) & 2i\gamma_{sp} \sin(k_x a) & 2i\gamma_{sp} \sin(k_y a) & 0 \\ -2i\gamma_{sp} \sin(k_x a) & E_{p_x}(\mathbf{k}) & 0 & 0 \\ -2i\gamma_{sp} \sin(k_y a) & 0 & E_{p_y}(\mathbf{k}) & 0 \\ 0 & 0 & 0 & E_{p_z}(\mathbf{k}) \end{pmatrix} \otimes \mathbb{I}_{2 \times 2}, \quad (\text{S3})$$

where

$$E_s(\mathbf{k}) = E_s - 2t_s [\cos(k_x a) + \cos(k_y a)], \quad (\text{S4a})$$

$$E_{p_x}(\mathbf{k}) = E_{p_x} + 2t_{p\sigma} \cos(k_x a) - 2t_{p\pi} \cos(k_y a), \quad (\text{S4b})$$

$$E_{p_y}(\mathbf{k}) = E_{p_y} - 2t_{p\pi} \cos(k_x a) + 2t_{p\sigma} \cos(k_y a), \quad (\text{S4c})$$

$$E_{p_z}(\mathbf{k}) = E_{p_z} - 2t_{p\pi} [\cos(k_x a) + \cos(k_y a)], \quad (\text{S4d})$$

and  $\mathbb{I}_{2 \times 2}$  is an identity operator in the spin space. Here, the basis states are

$$|\varphi_{l\sigma\mathbf{k}}^{(z)}\rangle = \sum_{\mathbf{R}} e^{i\mathbf{k}\cdot\mathbf{R}} |\phi_{l\sigma\mathbf{R}}^{(z)}\rangle, \quad (\text{S5})$$

where  $|\phi_{l\sigma\mathbf{R}}^{(z)}\rangle$  is a Wannier function localized at the Bravais lattice  $\mathbf{R} = (R_x, R_y)$  with its orbital character  $l = s, p_x, p_y, p_z$  and spin  $\sigma$ , which is defined in a layer located at  $z$ . For the Wannier states,  $E_s, E_{p_\alpha}$  are onsite energies for  $s$  and  $p_\alpha$  orbitals, and  $t_s, t_{p\sigma(\pi)}, \gamma_{sp}$  are the nearest hopping amplitudes between  $s$  orbitals, between  $p$  orbitals via  $\sigma(\pi)$  bonding, and between  $s$  and  $p$  orbitals, respectively. Second, the SOC part is

$$H_{\text{NM}}^{\text{so}} = \frac{\alpha_{\text{so}}^{\text{NM}}}{\hbar^2} \mathbf{L}^{(p)} \cdot \mathbf{S}, \quad (\text{S6})$$

where  $\mathbf{S}$  is the spin operator and  $\mathbf{L}^{(p)}$  is the orbital angular momentum (OAM) operator in  $p$  orbital space. Here,  $\alpha_{\text{so}}^{\text{NM}} > 0$  is the strength of the SOC in the NM. The OAM operator is explicitly expressed in a matrix representation

$$L_x^{(p)} = \hbar \begin{pmatrix} 0 & 0 & 0 \\ 0 & 0 & -i \\ 0 & i & 0 \end{pmatrix}, \quad L_y^{(p)} = \hbar \begin{pmatrix} 0 & 0 & i \\ 0 & 0 & 0 \\ -i & 0 & 0 \end{pmatrix}, \quad L_z^{(p)} = \hbar \begin{pmatrix} 0 & -i & 0 \\ i & 0 & 0 \\ 0 & 0 & 0 \end{pmatrix}, \quad (\text{S7})$$

with  $p_x, p_y$ , and  $p_z$  orbital Wannier functions. Finally, the interlayer coupling between neighboring NM layers is described as

$$T_{\text{NM}} = \begin{pmatrix} -t_{ss} & 0 & 0 & -\gamma_{sp} \\ 0 & -t_{p\pi} & 0 & 0 \\ 0 & 0 & -t_{p\pi} & 0 \\ \gamma_{sp} & 0 & 0 & t_{p\sigma} \end{pmatrix} \otimes \mathbb{I}_{2 \times 2}, \quad (\text{S8})$$

where the basis states for the row and column are  $\langle \varphi_{l\sigma\mathbf{k}}^{(z+1)} |$  and  $|\varphi_{l'\sigma'\mathbf{k}}^{(z)}\rangle$ , respectively, for  $z = 1, \dots, N_{\text{NM}} - 1$ .

## 2. FM

In the FM, we assume there are  $d_\beta$  ( $\beta = xy, yz, zx, x^2 - y^2, z^2$ ) orbitals at each site. The Hamiltonian within each two-dimensional layer is

$$H_{\text{FM}}^{(2d)}(\mathbf{k}) = H_{\text{FM}}^{\text{kin}}(\mathbf{k}) + H_{\text{FM}}^{\text{so}} + H_{\text{FM}}^{\text{xc}}, \quad (\text{S9})$$

where each term describes kinetic energy, SOC, and exchange interaction with magnetization, respectively. The kinetic energy term is

$$H_{\text{FM}}^{\text{kin}(2d)}(\mathbf{k}) = \begin{pmatrix} E_{d_{xy}}(\mathbf{k}) & 0 & 0 & 0 & 0 \\ 0 & E_{d_{yz}}(\mathbf{k}) & 0 & 0 & 0 \\ 0 & 0 & E_{d_{zx}}(\mathbf{k}) & 0 & 0 \\ 0 & 0 & 0 & E_{d_{x^2-y^2}}(\mathbf{k}) & 0 \\ 0 & 0 & 0 & 0 & E_{d_{z^2}}(\mathbf{k}) \end{pmatrix} \otimes \mathbb{I}_{2 \times 2}, \quad (\text{S10})$$



where

$$E_{d_{xy}}(\mathbf{k}) = E_{d_{xy}} + 2t_{d\pi} \cos(k_x a) + 2t_{d\pi} \cos(k_y a), \quad (\text{S11a})$$

$$E_{d_{yz}}(\mathbf{k}) = E_{d_{yz}} - 2t_{d\delta} \cos(k_x a) + 2t_{d\pi} \cos(k_y a), \quad (\text{S11b})$$

$$E_{d_{zx}}(\mathbf{k}) = E_{d_{zx}} + 2t_{d\pi} \cos(k_x a) - 2t_{d\delta} \cos(k_y a), \quad (\text{S11c})$$

$$E_{d_{x^2-y^2}}(\mathbf{k}) = E_{d_{x^2-y^2}} - [(3/2)t_{d\sigma} + (1/2)t_{d\delta}][\cos(k_x a) + \cos(k_y a)], \quad (\text{S11d})$$

$$E_{d_{z^2}}(\mathbf{k}) = E_{d_{z^2}} - [(1/2)t_{d\sigma} + (3/2)t_{d\delta}][\cos(k_x a) + \cos(k_y a)]. \quad (\text{S11e})$$

Here,  $E_{d_\beta}$  is the onsite energy of the  $d_\beta$  orbital, and  $t_{d\sigma}$ ,  $t_{d\pi}$ ,  $t_{d\delta}$  are nearest neighbor hoppings between  $d$  orbitals via  $\sigma$ ,  $\pi$ ,  $\delta$  bondings, respectively. The basis states are defined similarly as Eq. (S5) but for  $d_\beta$  orbital Wannier functions. The SOC term is

$$H_{\text{FM}}^{\text{so}} = \frac{\alpha_{\text{so}}^{\text{FM}}}{\hbar^2} \mathbf{L}^{(d)} \cdot \mathbf{S}, \quad (\text{S12})$$

where  $\alpha_{\text{so}}^{\text{FM}} > 0$  is the SOC strength. Here,  $\mathbf{L}^{(d)}$  is the OAM operator in  $d$  orbital space, whose matrix representation is written as

$$L_x^{(d)} = \hbar \begin{pmatrix} 0 & 0 & -i & -i & -\sqrt{3}i \\ 0 & 0 & 0 & 0 & 0 \\ i & 0 & 0 & 0 & 0 \\ i & 0 & 0 & 0 & 0 \\ \sqrt{3}i & 0 & 0 & 0 & 0 \end{pmatrix}, \quad L_y^{(d)} = \hbar \begin{pmatrix} 0 & i & 0 & 0 & 0 \\ -i & 0 & 0 & 0 & 0 \\ 0 & 0 & 0 & -i & \sqrt{3}i \\ 0 & 0 & i & 0 & 0 \\ 0 & 0 & -\sqrt{3}i & 0 & 0 \end{pmatrix}, \quad L_z^{(d)} = \hbar \begin{pmatrix} 0 & 0 & 0 & 2i & 0 \\ 0 & 0 & i & 0 & 0 \\ 0 & -i & 0 & 0 & 0 \\ -2i & 0 & 0 & 0 & 0 \\ 0 & 0 & 0 & 0 & 0 \end{pmatrix}, \quad (\text{S13})$$

where the basis states are  $d_{xy}$ ,  $d_{yz}$ ,  $d_{zx}$ ,  $d_{x^2-y^2}$ ,  $d_{z^2}$  orbital Wannier functions. The exchange interaction is

$$H_{\text{FM}}^{\text{xc}} = \frac{J}{\hbar} \hat{\mathbf{M}} \cdot \mathbf{S}, \quad (\text{S14})$$

where  $J > 0$  is the strength of the exchange interaction, and  $\hat{\mathbf{M}}$  is the direction of the magnetization. We assume  $\hat{\mathbf{M}} = \hat{\mathbf{z}}$  in the calculation. The interlayer coupling between neighboring FM layers is

$$T_{\text{FM}} = \begin{pmatrix} -t_{d\delta} & 0 & 0 & 0 & 0 \\ 0 & t_{d\pi} & 0 & 0 & 0 \\ 0 & 0 & t_{d\pi} & 0 & 0 \\ 0 & 0 & 0 & -t_{d\delta} & 0 \\ 0 & 0 & 0 & 0 & -t_{d\sigma} \end{pmatrix} \otimes \mathbf{I}_{2 \times 2}, \quad (\text{S15})$$

where the basis for the row and column are  $\langle \varphi_{l\sigma\mathbf{k}}^{(z+1)} |$  and  $|\varphi_{l'\sigma'\mathbf{k}}^{(z)}\rangle$ , respectively, for  $z = N_{\text{NM}} + 1, \dots, N_{\text{NM}} + N_{\text{FM}} - 1$ .

### 3. Interface

At the interface, there are hoppings between the last NM layer ( $z = N_{\text{NM}}$ ) and the first FM layer ( $z = N_{\text{NM}} + 1$ ), which are expressed in

$$T_{\text{interface}} = \begin{pmatrix} 0 & 0 & \gamma_{pd\pi} & 0 \\ 0 & 0 & \gamma_{pd\pi} & 0 \\ 0 & 0 & 0 & 0 \\ 0 & 0 & 0 & 0 \\ 0 & 0 & 0 & -\gamma_{pd\sigma} \end{pmatrix} \otimes \mathbf{I}_{2 \times 2}, \quad (\text{S16})$$

where the basis for the row and column are  $\langle \varphi_{l\sigma\mathbf{k}}^{(N_{\text{NM}}+1)} |$  and  $|\varphi_{l'\sigma'\mathbf{k}}^{(N_{\text{NM}})}\rangle$ , respectively. Here,  $\gamma_{pd\sigma(\pi)}$  is the nearest neighbor hopping between  $p$  and  $d$  orbitals via  $\sigma(\pi)$  hoppings. We neglect the hopping from a  $s$  orbital in the NM to  $d$  orbitals in the FM, since the  $s$  orbital does not carry the OAM, thus not affecting the orbital injection.

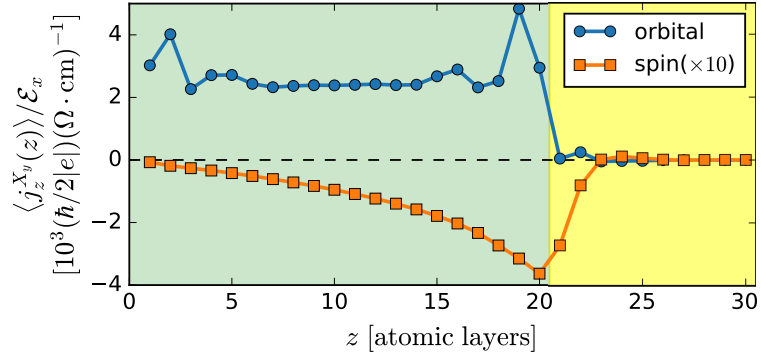


FIG. S1. Spatial profiles of the orbital (blue circles) and spin (orange squares, 10x enlarged) Hall currents in the NM region ( $1 \leq z \leq 20$ ) and the FM region ( $21 \leq z \leq 30$ ). The Fermi energy is set to  $E_F = -0.9$  eV.

#### 4. Parameter Setting

For the tight-binding model defined above, parameters which we used for the calculation in Figs. 2 and 3 of the Letter are set as

$$E_s = 3.2, E_{p_x} = E_{p_y} = E_{p_z} = -0.5, t_s = 0.5, t_{p\sigma} = 0.5, t_{p\pi} = 0.2, \gamma_{sp} = 0.5, \alpha_{\text{so}}^{\text{NM}} = 0, \quad (\text{S17})$$

for the NM,

$$E_{d_{xy}} = E_{d_{yz}} = E_{d_{zx}} = E_{d_{x^2-y^2}} = E_{d_{z^2}} = -0.5, t_{d\sigma} = 0.1, t_{d\pi} = 0.05, t_{d\delta} = 0.02, J = 0.5, \alpha_{\text{so}}^{\text{FM}} = 0.1 \quad (\text{S18})$$

for the FM, and

$$\gamma_{pd\sigma} = 0.4, \gamma_{pd\pi} = 0.1 \quad (\text{S19})$$

for the interface. All parameters are expressed in unit of eV.

### B. Spatial Profiles of the Orbital and Spin Hall Currents

Linear responses of the orbital and spin Hall currents are evaluated using the Kubo formula as follows:

$$\langle \delta j_z^{X_y}(z) \rangle = -e\hbar\mathcal{E}_x \sum_{nm} \int \frac{d^2k}{(2\pi)^2} (f_{n\mathbf{k}} - f_{m\mathbf{k}}) \text{Im} \left[ \frac{\langle u_{n\mathbf{k}} | j_z^{X_y}(z) | u_{m\mathbf{k}} \rangle \langle u_{m\mathbf{k}} | v_x | u_{n\mathbf{k}} \rangle}{(E_{n\mathbf{k}} - E_{m\mathbf{k}} + i\Gamma)^2} \right], \quad (\text{S20})$$

where

$$j_z^{X_y}(z) = \frac{1}{2} \sum_{z'} \left[ P(z') \frac{1}{2} \{v_z, X_y\} P(z) + P(z) \frac{1}{2} \{v_z, X_y\} P(z') \right] \quad (\text{S21})$$

is the spin/orbital ( $\mathbf{X} = \mathbf{L}$  or  $\mathbf{S}$ ) current operator defined in a layer at  $z$ . Here,  $P(z)$  is the projection operator to a layer at  $z$ . The velocity operator along the  $z$  direction is defined as

$$v_z = \frac{1}{i\hbar} \sum_{zz'} (z - z') P(z) H P(z'). \quad (\text{S22})$$

Figure S1 shows spatial profiles of the orbital and spin Hall currents obtained from the tight-binding model introduced in Sec. . The parameters are set as Eqs. (S17)-(S19), and the numbers of the NM and FM layers are  $N_{\text{NM}} = 20$  and  $N_{\text{FM}} = 10$ . For this calculation, we set the Fermi energy as  $E_F = -0.9$  eV. We find that the orbital Hall conductivity in the NM region is more than  $\approx 2,000 (\hbar/2|e|)(\Omega\text{cm})^{-1}$ . In the FM region, part of the orbital Hall current is injected, which is converted to the spin current by the SOC of the FM [Eq (S12)]. We also find the spin current in the NM region, which is decaying from the interface. This is because reflected current from the interface becomes spin-polarized. The decay is due to finite spectral broadening  $\Gamma = 25$  meV in Eq. (S20).

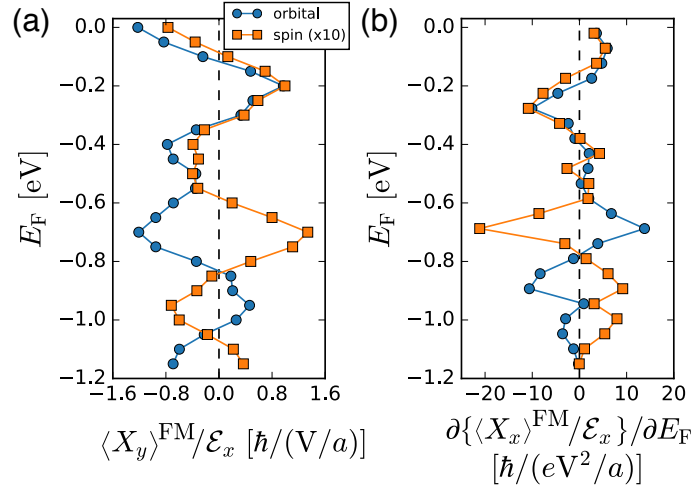


FIG. S2. Fermi energy ( $E_F$ ) dependences of (a)  $\langle X_y \rangle^{\text{FM}} / \mathcal{E}_x$  and (b)  $\partial\{\langle X_x \rangle^{\text{FM}} / \mathcal{E}_x\} / \partial E_F$ . For this calculation, the numbers of each layers are set to  $N_{\text{NM}} = 8$  and  $N_{\text{FM}} = 2$ .

### C. Correlation between $\langle X_y \rangle^{\text{FM}}$ and $\langle X_x \rangle^{\text{FM}}$ ( $X = L, S$ ): Fermi Energy Dependence

Figure S2(a) shows Fermi energy dependence of  $\langle X_y \rangle^{\text{FM}} / \mathcal{E}_x$  for  $N_{\text{NM}} = 8$  and  $N_{\text{FM}} = 2$ , where  $X = L$  or  $S$ . This contribution is even under the sign reversal of  $\hat{\mathbf{M}}$ , and arises from the intraband contribution [Eq. (2a) of the Letter]. While sign and magnitude vary depending on  $E_F$ , the signs of  $\langle L_y \rangle^{\text{FM}}$  and  $\langle S_y \rangle^{\text{FM}}$  are opposite in the lower energy range ( $-1.2 \lesssim E_F \lesssim -0.6$ ) and same in the upper energy range ( $-0.5 \lesssim E_F \lesssim 0$ ). The  $E_F$ -dependence of the sign of the relative ratio between  $\langle L_y \rangle^{\text{FM}}$  and  $\langle S_y \rangle^{\text{FM}}$  strikingly resembles the energy dependence of the spin-orbit correlation  $\langle \mathbf{L} \cdot \mathbf{S} \rangle_{\text{eq}}^{\text{FM}}$  in Fig. 2(b).

However, the variation of  $\langle X_y \rangle^{\text{FM}} / \mathcal{E}_x$  [Fig. S2(a)] differs from the variation of  $\langle X_x \rangle^{\text{FM}} / \mathcal{E}_x$  [Fig. 4(a)]. A reason for such difference is due to the fact that while  $\langle X_y \rangle^{\text{FM}}$  arises from the *intraband* contribution for the states at the Fermi *surface* [Eq. 2(a)]  $\langle X_x \rangle^{\text{FM}}$  arises from the *interband* contribution for the states in the Fermi *sea* [Eq. 2(b)]. However, for each state in the band structure, they have strong correlations. To demonstrate this point, we present in Fig. S2(b) a plot of  $\partial\{\langle X_x \rangle^{\text{FM}} / \mathcal{E}_x\} / \partial E_F$ , which corresponds to the contribution within the energy slice near  $E_F$ . By comparing this with  $\langle X_y \rangle^{\text{FM}} / \mathcal{E}_x$  [Fig. S2(a)], we find strong resemblance for both orbital and spin over the whole range of  $E_F$ , except that their relative signs are opposite.

### D. Spin-Orbit Coupling Dependence

Figure S3 shows Fermi energy dependences of (a)  $\langle L_y \rangle^{\text{FM}} / \mathcal{E}_x$ , (b)  $\langle S_y \rangle^{\text{FM}} / \mathcal{E}_x$ , (c)  $\langle L_x \rangle^{\text{FM}} / \mathcal{E}_x$ , and (d)  $\langle S_x \rangle^{\text{FM}} / \mathcal{E}_x$  for different values of  $\alpha_{\text{so}}^{\text{FM}}$ . First,  $\langle L_y \rangle^{\text{FM}} / \mathcal{E}_x$  remains almost invariant under the increase of  $\alpha_{\text{so}}^{\text{FM}}$  [Fig. S3(a)]. This is expected because  $\langle L_y \rangle^{\text{FM}}$ , which results from the orbital Hall effect (OHE) in the NM, is not affected by the SOC of the FM. On the other hand, the rest three quantities exhibit monotonic increase as  $\alpha_{\text{so}}^{\text{FM}}$  becomes larger within the range  $\alpha_{\text{so}}^{\text{FM}} \leq 200$  meV [Figs. S3(b), S3(c), and S3(d)]. The monotonic increase of  $\langle S_y \rangle^{\text{FM}} / \mathcal{E}_x$  [Fig. S3(b)] is understandable because  $\langle S_y \rangle^{\text{FM}}$  is directly converted from the  $\langle L_y \rangle^{\text{FM}}$  by the SOC in the FM. Also, since  $\langle S_x \rangle^{\text{FM}}$  results from the precession of  $\langle S_y \rangle^{\text{FM}}$  by the exchange interaction in the FM [Eq. (S14)], monotonic increase of the  $\langle S_x \rangle^{\text{FM}} / \mathcal{E}_x$  with  $\alpha_{\text{so}}^{\text{FM}}$  follows that of  $\langle S_y \rangle^{\text{FM}} / \mathcal{E}_x$  [Fig. S3(d)]. On the other hand, since the precession of the spin is coupled to the orbital by the SOC in the FM,  $\langle L_x \rangle^{\text{FM}} / \mathcal{E}_x$  is proportional to  $\langle S_x \rangle^{\text{FM}} / \mathcal{E}_x$ . Thus,  $\langle L_x \rangle^{\text{FM}} / \mathcal{E}_x$  also increases monotonically with increasing  $\alpha_{\text{so}}^{\text{FM}}$  [Fig. S3(c)].

In Fig. 4(b), the SOC dependence of  $\langle \tau_d \rangle^{\text{FM}} / \mathcal{E}_x$ , which is proportional to  $\langle S_x \rangle^{\text{FM}} / \mathcal{E}_x$ , is shown for fixed Fermi energies  $E_F = -0.15$  eV and  $E_F = -0.80$  eV. In Fig. S3(d), we find that  $\langle S_x \rangle^{\text{FM}} / \mathcal{E}_x$  monotonically increases with  $\alpha_{\text{so}}^{\text{FM}}$  at  $E_F = -0.15$  eV and  $E_F = -0.80$  eV. Although the magnitude of the peak monotonically increases, the peak position may change at some Fermi energy, i.e. at  $E_F = -0.75$  eV. At such Fermi energy,  $\langle S_x \rangle^{\text{FM}} / \mathcal{E}_x$  may exhibit nonmonotonic behavior. This is due to modification of the band structure with increasing  $\alpha_{\text{so}}^{\text{FM}}$ .

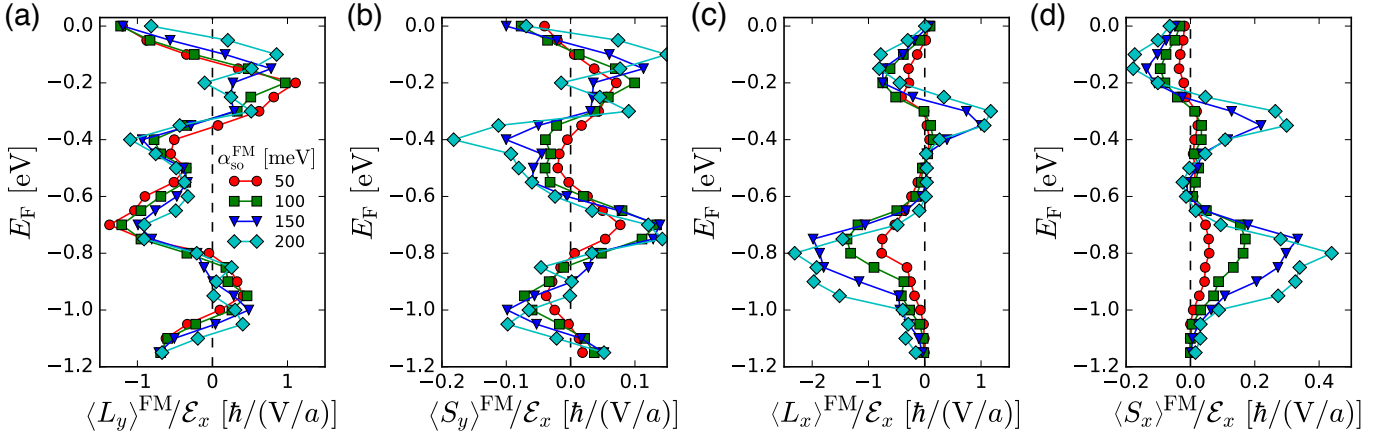


FIG. S3.  $E_F$ -dependences of (a)  $\langle L_y \rangle^{\text{FM}} / \mathcal{E}_x$ , (b)  $\langle S_y \rangle^{\text{FM}} / \mathcal{E}_x$ , (c)  $\langle L_x \rangle^{\text{FM}} / \mathcal{E}_x$ , and (d)  $\langle S_x \rangle^{\text{FM}} / \mathcal{E}_x$  for different values of  $\alpha_{\text{so}}^{\text{FM}}$ . For this calculation, the numbers of each layers are set to  $N_{\text{NM}} = 8$  and  $N_{\text{FM}} = 2$ .

## E. Orbital Torque versus Spin Torque

### 1. NM SOC included

When the SOC in the NM is nonzero, the spin Hall effect (SHE) follows the OHE [S1] thus orbital torque (OT) and spin torque (ST) coexist. Relative sign of the OT and ST is determined by the spin-orbit correlations  $\langle \mathbf{L} \cdot \mathbf{S} \rangle_{\text{eq}}^{\text{NM}}$  in the NM and  $\langle \mathbf{L} \cdot \mathbf{S} \rangle_{\text{eq}}^{\text{FM}}$  in the FM as summarized in Table I of the Letter. In this section, we demonstrate this point from the numerical calculation by setting finite SOC strength in the NM:

$$\alpha_{\text{so}}^{\text{NM}} = 0.2 \text{ eV}. \quad (\text{S23})$$

Except for  $\alpha_{\text{so}}^{\text{NM}}$ , the rest of the parameters are set equal to Eqs. (S17), (S18), and (S19). Figure S4 displays the band structure shown in lines and (a)  $\langle \mathbf{L} \cdot \mathbf{S} \rangle_{\text{eq}}^{\text{NM}}$  and (b)  $\langle \mathbf{L} \cdot \mathbf{S} \rangle_{\text{eq}}^{\text{FM}}$  shown in colors. In the NM,  $\langle \mathbf{L} \cdot \mathbf{S} \rangle_{\text{eq}}^{\text{NM}}$  is positive in the upper energy range ( $-0.5 \text{ eV} \lesssim E_{n\mathbf{k}} \lesssim 0.0 \text{ eV}$  near the  $\Gamma$ -point and  $-0.8 \text{ eV} \lesssim E_{n\mathbf{k}} \lesssim 0.0 \text{ eV}$  near the M-point) and negative in the lower energy range ( $-1.2 \text{ eV} \lesssim E_{n\mathbf{k}} \lesssim -0.6 \text{ eV}$  near the  $\Gamma$ -point and  $-1.2 \text{ eV} \lesssim E_{n\mathbf{k}} \lesssim -0.9 \text{ eV}$  near the M-point) in general [Fig. S4(a)]. Note that this is essentially the same as Fig. 2(b) of Ref. [S1] because all the parameters in the NM regions are set equal to those used in Ref. [S1]. Meanwhile,  $\langle \mathbf{L} \cdot \mathbf{S} \rangle_{\text{eq}}^{\text{FM}}$  in Fig. S4(b) is almost the same as Fig. 2(b) of the Letter.

In order to differentiate the OT and ST contributions to  $\langle \mathbf{S}(z) \rangle$ , we calculate electric field response of  $\langle \mathbf{S}(z) \rangle$  [Eq. (2) of the

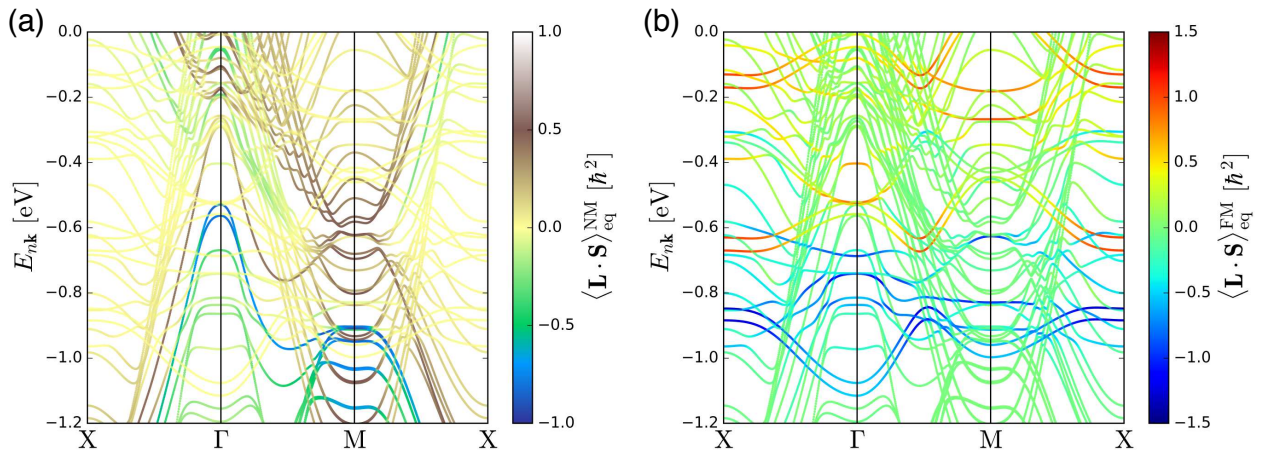


FIG. S4. Band structure and the spin-orbit correlations in the (a) NM and (b) FM regions, when the SOC included in both regions. For this calculation, we assumed  $N_{\text{NM}} = 8$  and  $N_{\text{FM}} = 2$ .



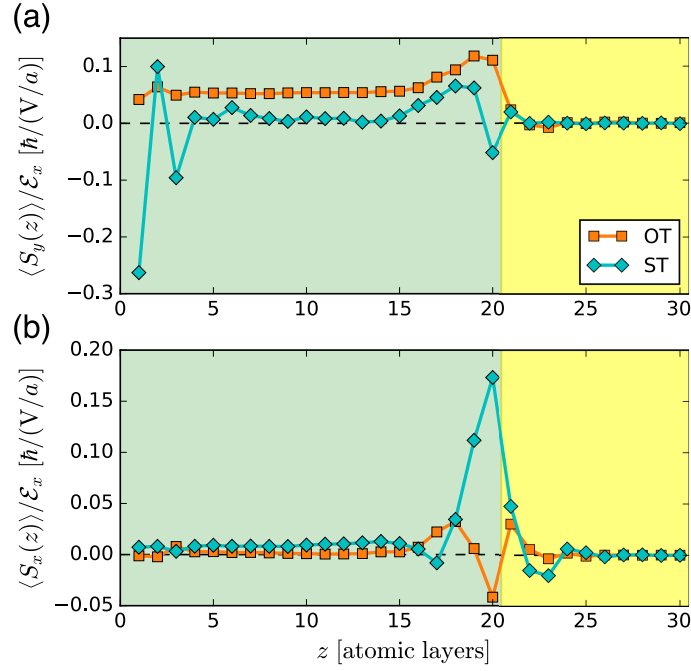


FIG. S5. Spatial profiles of (a)  $\langle S_y \rangle / \mathcal{E}_x$  and (b)  $\langle S_x \rangle / \mathcal{E}_x$  in the NM ( $1 \leq z \leq 20$ ) and FM ( $21 \leq z \leq 30$ ) regions. The OT and ST contributions are represented by orange squares and cyan diamonds, respectively. The SOC is included in the NM by Eq. (S23) and the corresponding band structure is shown in Fig. S4. The Fermi energy is set equal to  $E_F = -0.9$  eV.

Letter] by setting SOC strength parameters in the NM and FM by (i)  $\alpha_{\text{so}}^{\text{NM}} = 0.2$  eV,  $\alpha_{\text{so}}^{\text{FM}} = 0.1$  eV, and (ii)  $\alpha_{\text{so}}^{\text{NM}} = 0.2$  eV,  $\alpha_{\text{so}}^{\text{FM}} = -0.1$  eV. Note that the sign of  $\alpha_{\text{so}}^{\text{FM}}$  is reversed in (ii). This reversal is motivated by the fact that it reverses the sign of the OT while it does not affect the sign of the ST. By this way, the band structure is barely affected and also the sign of the  $\langle \mathbf{L} \cdot \mathbf{S} \rangle_{\text{eq}}^{\text{FM}}$  for the case (ii) becomes opposite to that for the case (i). Thus, we define the OT and ST contributions as

$$\langle \mathbf{S}(z) \rangle_{\text{OT}} = \frac{1}{2} \left[ \langle \mathbf{S}(z) \rangle_{(i)} - \langle \mathbf{S}(z) \rangle_{(ii)} \right], \quad (\text{S24a})$$

$$\langle \mathbf{S}(z) \rangle_{\text{ST}} = \frac{1}{2} \left[ \langle \mathbf{S}(z) \rangle_{(i)} + \langle \mathbf{S}(z) \rangle_{(ii)} \right], \quad (\text{S24b})$$

such that  $\langle \mathbf{S}(z) \rangle_{(i)} = \langle \mathbf{S}(z) \rangle_{\text{OT}} + \langle \mathbf{S}(z) \rangle_{\text{ST}}$ . Therefore, we calculate  $\langle \mathbf{S}(z) \rangle_{(i)}$  and  $\langle \mathbf{S}(z) \rangle_{(ii)}$  from the Kubo formula in Eq. (2) of the Letter, and extract the OT and ST contributions by Eq. (S24) for  $E_F = -0.9$  eV, where  $\langle \mathbf{L} \cdot \mathbf{S} \rangle_{\text{eq}}^{\text{NM}} < 0$  and  $\langle \mathbf{L} \cdot \mathbf{S} \rangle_{\text{eq}}^{\text{FM}} < 0$  [Fig. S4]. Thus, the OT and ST contributions are expected to have the same sign.

In Fig. S5(a), spatial profile of  $\langle S_y(z) \rangle / \mathcal{E}_x$  is shown in the NM region ( $1 \leq z \leq 20$ ) and the FM region ( $21 \leq z \leq 30$ ). The OT contribution (orange squares) is similar to the result of  $\langle S_y(z) \rangle / \mathcal{E}_x$  when  $\alpha_{\text{so}}^{\text{NM}} = 0$  [Fig. 3(a) of the Letter]. On the other hand, the ST contribution (cyan diamonds) exhibits a standard behavior of the SHE; the spin is accumulated at the boundary. Near  $z = 1$ , sign of  $\langle S_y(z) \rangle / \mathcal{E}_x$  is negative, which implies that the OHE and SHE occurs in the opposite directions. In the absence of the FM,  $\langle S_y(z) \rangle / \mathcal{E}_x$  is positive near  $z = 20$  (not shown). However, due to presence of the FM attached,  $\langle S_y(z) \rangle / \mathcal{E}_x$  is reduced near  $z = 20$ , which is injected to the FM. We find that the signs of the OT and ST contributions are same in the FM region. This is expected from the spin-orbit correlations of states near  $E = -0.9$  eV and from the fact that  $\langle S_y(z) \rangle / \mathcal{E}_x$  results from the intraband contribution at the Fermi surface [Eq. (2a)]. When  $\langle S_y \rangle$  is injected to the FM, it precesses along the magnetization by the exchange interaction, regardless of whether it is the OT or ST contribution. In the Kubo formula calculation,  $\langle S_x(z) \rangle / \mathcal{E}_x$  is captured by the interband contribution in the Fermi sea [Eq. (2b) of the Letter]. Nevertheless, we find that the signs of the OT and ST contributions are same in the FM region [Fig. S5(b)], which is because *all the states* below  $E_F = -0.9$  eV satisfy  $\langle \mathbf{L} \cdot \mathbf{S} \rangle_{\text{eq}}^{\text{NM}} < 0$  and  $\langle \mathbf{L} \cdot \mathbf{S} \rangle_{\text{eq}}^{\text{FM}} < 0$ .

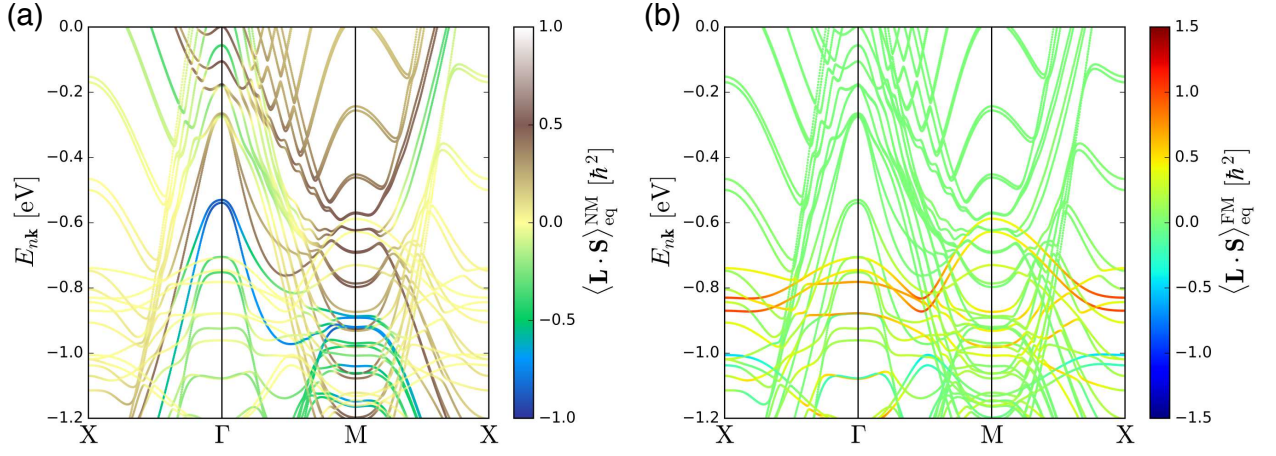


FIG. S6. Band structure and the spin-orbit correlations in the (a) NM and (b) FM regions, when the SOC included in both regions and the  $d$  orbitals onsite energies in the FM are lowered by 0.7 eV. For this calculation, we assumed  $N_{\text{NM}} = 8$  and  $N_{\text{FM}} = 2$ .

## 2. NM SOC included, FM onsite changed

The result shown in the previous subsection considers the case when the sign of the OT and ST is same. In this subsection, we present a result in another regime where the OT and ST have the opposite signs. To achieve this, we shift the onsite energy of  $d$  orbitals in the FM by setting

$$E_{d_{xy}} = E_{d_{yz}} = E_{d_{zx}} = E_{d_{x^2-y^2}} = E_{d_{z^2}} = -1.2 \text{ eV}, \quad (\text{S25})$$

which is lower than the original system by 0.7 eV [Eq. (S18)]. The rest of the parameters are unchanged. The spin-orbit correlations in the NM and FM are shown on top of the band structure in Figs. S6(a) and S6(b), respectively. Now near

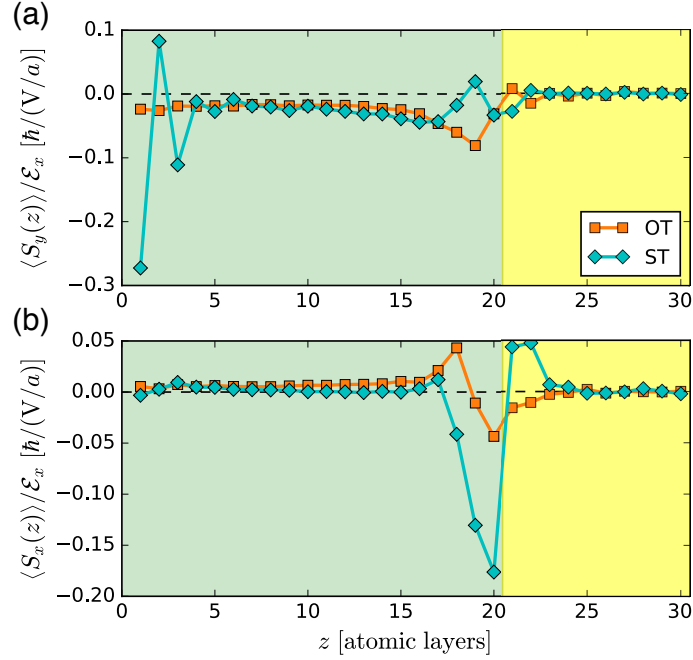


FIG. S7. Spatial profiles of (a)  $\langle S_y \rangle / \mathcal{E}_x$  and (b)  $\langle S_x \rangle / \mathcal{E}_x$  in the NM ( $1 \leq z \leq 20$ ) and FM ( $21 \leq z \leq 30$ ) regions. The OT and ST contributions are represented by orange squares and cyan diamonds, respectively. The SOC is included in the NM by Eq. (S23) and the onsite energies of the  $d$  orbitals in the FM is shifted by Eq. (S25). The corresponding band structure is shown in Fig. S6. The Fermi energy is set equal to  $E_F = -0.9$  eV.

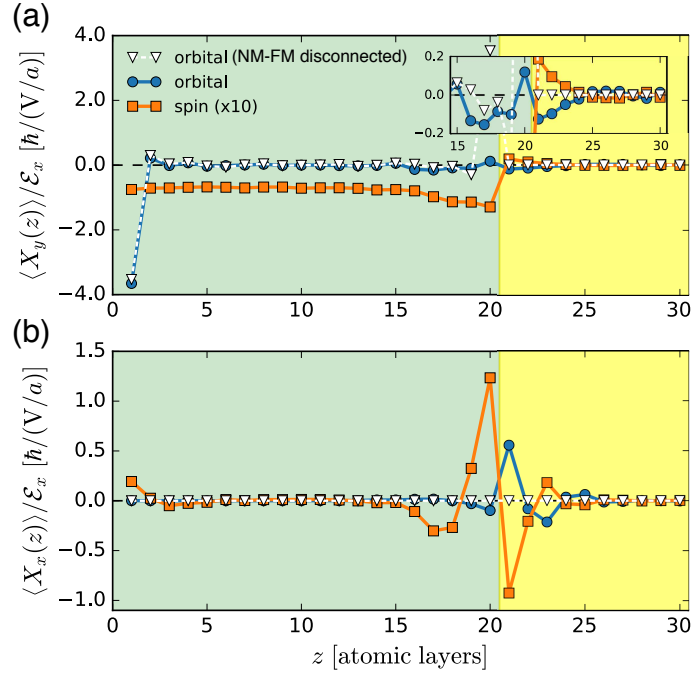


FIG. S8. (a)  $\langle X_y(z) \rangle / \mathcal{E}_x$  and (b)  $\langle X_x(z) \rangle / \mathcal{E}_x$  as a function of  $z$  for  $E_F = -0.9$  eV, when the relative sign of the interface hoppings is flipped [Eq. (S27)]. Blue circles (orange squares) depict the orbital (spin multiplied by factor 10) accumulation profile in the NM ( $1 \leq z \leq 20$ ) and the FM ( $21 \leq z \leq 30$ ). White inverted triangles depict the orbital accumulation profile when the NM and FM are disconnected. The inset in (a) presents a magnified plot near the NM/FM interface.

$E_F = -0.9$  eV,  $\langle \mathbf{L} \cdot \mathbf{S} \rangle_{\text{eq}}^{\text{NM}} < 0$  but  $\langle \mathbf{L} \cdot \mathbf{S} \rangle_{\text{eq}}^{\text{FM}} > 0$ , thus we expect the opposite signs for the OT and ST. From the same method [Eq. (S24)], we calculate the electric field responses of the OT and ST contributions. Figures S7(a) and S7(b) show the results for  $\langle S_y(z) \rangle / \mathcal{E}_x$  and  $\langle S_x(z) \rangle / \mathcal{E}_x$ , respectively. We find the signs of the OT and ST contributions are opposite in both cases. The result for  $\langle S_x(z) \rangle$  [Fig. S7(b)], which is the interband contribution from the Fermi sea, is understood as the following. Although there are many FM bands with  $\langle \mathbf{L} \cdot \mathbf{S} \rangle_{\text{eq}}^{\text{FM}} < 0$  below  $E_F = -0.9$  eV, the hotspots for the OHE and SHE in the NM is concentrated in the energy range  $-1.0$  eV  $\lesssim E_{n\mathbf{k}} \lesssim 0.0$  eV [S1] thus the torque contribution from the FM bands with  $\langle \mathbf{L} \cdot \mathbf{S} \rangle_{\text{eq}}^{\text{FM}} < 0$  is negligible and the major contribution is from the states in an energy range  $-1.0$  eV  $\lesssim E_{n\mathbf{k}} \lesssim -0.9$  eV.

### F. Role of the Interface Hoppings for the Orbital Torque

In this section, we demonstrate crucial role of the interface hoppings for the OT. For the orbital injection from the NM to the FM in the tight-binding model presented in the Letter, the orbital information in the  $p$  orbitals in the NM should be transferred to the  $d$  orbitals in the FM. At the interface, two types of hoppings are crucial for this:

$$t_{pd}^\sigma = \langle p_z^{\text{NM}} | H_{\text{hop}} | d_{z^2-x^2}^{\text{FM}} \rangle, \quad (\text{S26a})$$

$$t_{pd}^\pi = \langle p_x^{\text{NM}} | H_{\text{hop}} | d_{zx}^{\text{FM}} \rangle. \quad (\text{S26b})$$

Once a state carrying finite OAM,  $|L_y^{(p)} = \pm 1\rangle = |p_z\rangle \pm i|p_x\rangle$  for example, is induced in the NM, the interface hoppings in Eq. (S26) can generate a state  $|L_y^{(d)} = \pm 2\rangle = |d_{z^2-x^2}^{\text{FM}}\rangle \pm i|d_{zx}^{\text{FM}}\rangle$  that also carries net OAM.

Thus, the relative sign of  $\gamma_{pd\sigma}$  and  $\gamma_{pd\pi}$  is crucial, by which the OT changes the sign. In the tight-binding model used in the Letter, we assume the same sign for  $\gamma_{pd\sigma}$  and  $\gamma_{pd\pi}$  [Eq. (S19)]. In order to demonstrate this effect, we present calculation results for  $\langle X_y(z) \rangle / \mathcal{E}_x$  and  $\langle X_x(z) \rangle / \mathcal{E}_x$  in Figs. S8(a) and S8(b), respectively, by assuming

$$\gamma_{pd\sigma} = -0.4, \quad \gamma_{pd\pi} = 0.1, \quad (\text{S27})$$

which is to be compared with Fig. 3 of the Letter. We find that  $\langle L_y(z) \rangle / \mathcal{E}_x$  is unchanged near  $z = 1$ , which is away from the interface. However, near the interface ( $z = 20$ ) and in the FM region ( $21 \leq z \leq 30$ ), the sign of the  $\langle L_y(z) \rangle / \mathcal{E}_x$  in Fig. S8(a) is opposite to that in Fig. 3(a) of the Letter. As a consequence,  $\langle S_y(z) \rangle / \mathcal{E}_x$ , which is converted from the injected orbital angular

momentum, also changes the sign [Fig. S8(a)]. Since  $\langle S_x(z) \rangle / \mathcal{E}_x$  precesses along the magnetization by the exchange interaction and  $\langle L_x(z) \rangle / \mathcal{E}_x$  follows by the SOC in the FM, the signs of  $\langle L_x(z) \rangle / \mathcal{E}_x$  and  $\langle S_x(z) \rangle / \mathcal{E}_x$  in Fig. S8(b) are flipped compared to Fig. 3(b) of the Letter.

Therefore, the interface crystallinity is crucial for the generation of the OT. In dirty interface, the interface hoppings, such as Eq. (S26), are randomized, and this reduces the magnitude of the OT. On the other hand, the spin injection is not affected by the relative sign of the interface hoppings, thus the ST is less susceptible to the interface crystallinity.

---

\* hwl@postech.ac.kr

[S1] D. Go, D. Jo, C. Kim, and H.-W. Lee, Phys. Rev. Lett. **121**, 086602 (2018).